Mathematical Modelling and Numerical Simulation with Applications, 2025, 5(2), 451–471

https://dergipark.org.tr/en/pub/mmnsa
ISSN Online: 2791-8564 / Open Access
https://doi.org/10.53391/mmnsa.1548410

RESEARCH PAPER

Flow of non-Newtonian fluid with convective conditions in Darcy-Forchheimer media: an unsteady case

Touseef Fayaz [1,‡], **Mohammad Sharifuddin Ansari** [1,*,‡], **Olumuyiwa Otegbeye** [2,‡] **and Mumukshu Trivedi** [3,‡]

[1]School of Technology, Pandit Deendayal Energy University, Gandhinagar - 382421, India, [2]School of Computer Science and Applied Mathematics, Faculty of Science, University of the Witwatersrand, Johannesburg, Gauteng, South Africa, [3]Institute of Management, Nirma University, Ahmedabad, Gujarat

* Corresponding Author
‡ touseef.fphd21@sot.pdpu.ac.in (Touseef Fayaz); shariffuddin@gmail.com (Md. S. Ansari); Olumuyiwa.otegbeye@wits.ac.za (Olumuyiwa Otegbeye); mumukshu11@gmail.com (Mumukshu Trivedi)

Abstract

This research investigates the transient hydromagnetic behavior and heat transfer attributes of a non-Newtonian Casson nanoliquid embedded with microorganisms, flowing past a stretched surface in a Darcy-Forchheimer medium. The effect of a magnetic field, oriented at an angle α with the boundary surface, Joule dissipation, and convective boundary conditions are considered to determine the flow behavior, heat transfer, nanoparticle concentration, and microorganism density. To solve the non-dimensionalized system of coupled and nonlinear partial differential equations, the bivariate spectral quasi-linearization method (BSQLM) is employed. This numerical scheme has proven to be both convergent and accurate. Outcomes are compared with the results available in the literature and found good agreement. Variations in flow, heat transfer, distribution of nanoparticles, and microorganisms are illustrated by reproducing the numerical results in graphical form, whereas Nusselt and Sherwood numbers are displayed in tables. The Casson parameter uniformly diminishes the velocity and temperature inside the boundary layer region. Angle of inclination (α) boosts the temperature profile near the boundary and decreases the fluid velocity and nanoparticle concentration. The Prandtl number gives a rise in temperature near the wall and reveals an opposite effect away from the thermal boundary layer region. The Lewis number exerts a diminishing impact on the nanoparticle concentration field. Eckert number thickens the thermal boundary layer region. The microbe density field is a decreasing function of Peclet number. Solutal, thermal, and microorganism biot number exert, respectively, an enhancing effect on nanoparticle concentration, a diminishing influence on temperature profile, and a microbe density. This model is valuable for understanding the applications of solar energy in thermal engineering processes and has direct implications for industries such as glass and polymer manufacturing, thermal exchangers, homogenization, biomedical engineering, nuclear reactors, and metallic plate cooling.

Keywords: Casson nanofluid; magnetic field; microorganism; spectral quasi-linearisation method;

bioconvection; convective conditions

AMS 2020 Classification: 76A05; 76M22; 76W05

1 Introduction

Enhancement of thermophysical properties due to the inclusion of nanoparticles in a fluid is well documented in the literature. The nanoparticles, which can be metals, oxides, or nanotubes, can be incorporated into various fluids in order to achieve significant improvement in thermal conductivity and heat transfer performance. Non-Newtonian attributes in nanofluids are particularly important owing to their extensive applications in chemical, mechanical, and bioengineering industries. Processes such as cooling, heating, and homogenization can influence rheological properties of fluid, thereby affecting its overall characteristics [1–5]. Non-Newtonian behavior arises due to deviations in the standard stress-strain rate relationship, allowing shear stress to vary with its rate or change with primary force. Numerous non-Newtonian models were established to describe various types of behavior, like Bingham plastic, Herschel-Bulkley, and power law models being among the most notable.

The Casson model explains the rheological behavior of various fluids, including blood, cornstarch syrup, toothpaste, ketchup, chocolate, and honey. Similar to the Bingham model, the Casson model incorporates yield stress or critical shear stress, with the transition from a solid to a fluid occurring when the shear stress surpasses the critical threshold. The study of boundary layer flow near a stretching boundary is a captivating topic with numerous applications. Understanding the nonlinear behavior of Casson fluids over stretching boundaries is essential in fields like polymer extrusion, particularly within porous media. The interaction between yield stress, shear-thinning properties, and porous medium characteristics is crucial for the efficiency and quality of the extrusion process. Practical application of magnetic forces oblige the Casson fluid model relevant in the fields of engineering, such as plasma fusion technology, magnetohydrodynamic reactors, polymer engineering, and crude oil refinement [6, 7]. The following papers [8–10] deal with the magnetohydrodynamics mixed convection flow in a non-Darcy porous medium, considering various flow aspects and different geometries.

Bacteria are the primary drivers of bioconvection, a phenomenon where fluid motion is induced by density gradients created by the directed movement of motile microorganisms. The patterns of bioconvection vary based on the motility mechanisms of different microbes, classified into gyrotactic, chemotactic, and oxytactic microorganisms, etc. While all these types share a fundamental bio-convection mechanism, they exhibit distinct taxa. Kuznetsov [11] formulated a theory of bio-thermal convection in a suspension containing two types of microorganisms, gyrotactic and oxytactic, each exhibiting distinct taxis behaviors. This theory was utilized to explore the onset of bio-thermal convection within a horizontally layered suspension of finite depth. This phenomenon is significant in numerous industrial processes and chemical processing, such as extrusion, conveyor belt operations, polymer sheet production, surface change technology, biological procedures and chemical processing, prompting researchers to focus on enhancing mass transfer rates and species concentration in these systems. Raju and Sandeep [12] reported that temperature and mass exchange rates are increasing functions of buoyancy parameters and Biot number in MHD Casson bio-convective nanofluid flow. It is also concluded that bio-convective flow achieves higher heat and mass transfer efficiency over a rotating plate than over a rotating cone. Raju and Sandeep [13] conducted a numerical study on the flow of magnetohydrodynamics

➤ **Received:** 11.09.2024 ➤ **Revised:** 13.06.2025 ➤ **Accepted:** 21.06.2025 ➤ **Published:** 30.06.2025

Casson fluid with gyrotactic microbes in a porous medium over vertical spinning cones/plates. Ray et al. [14] examined the time-dependent laminar magnetohydrodynamic bioconvective flow and heat transfer of an electrically conducting non-Newtonian Casson thin film with constant thickness, considering viscous dissipation and the Buongiorno nanoscale model. Oyelakin et al. [15] investigated the flow of an electrically conducting Casson nanofluid with gyrotactic microorganisms over a moving wedge with nonlinear radiation and variable transport properties. Saeed and Gul [16] investigated Darcy-Forchheimer bioconvective flow of a Casson nanofluid over a rotating disk, incorporating the effects of Arrhenius activation energy and thermal radiation. Sanjalee et al. [17] carried out an analysis on the eigenvalue problem related to thermal instability in the flow of Casson nanofluid with aerobic microorganisms. Khan et al. [18] studied the Casson nanofluid flow over a stretching porous surface in the presence of microorganisms, Joule heating, and thermal Robin condition. Sankari et al. [19] presented a theoretical analysis of hydromagnetic bioconvective Casson nanofluid with motile microorganism near a stretching permeable surface in a porous medium with radiation and chemical reaction. Patil and Benawadi [20] analyzed the MHD bioconvective flow of Casson-Williamson nanoliquid with oxytactic microbes near a cylinder. Sagadevan et al. [21] investigated the flow of a Casson nanofluid due to a spinning disc in the presence of microorganisms and chemical reaction. Dharmaiah et al. [22] presented an analysis dealing with the flow of Carreau nanofluid along with microorganism in the vicinity of permeable cone-wedge geometry, considering the effects of thermal radiation, non-uniform heat source/sink, chemical reaction, and Cattaneo-Christov heat flux.

The present literature survey highlights a gap in studies focusing on heat and mass transfer analysis under temperature, mass, and microorganism density convective conditions at the surface. Notably, there has been no investigation into how these convective conditions influence the density of microorganisms at the boundary in unsteady Casson fluid flow with nanoparticles. This study aims to fill that gap by exploring these conditions and presenting new findings. The primary objective is to scrutinize the heat and mass transfer of unsteady Casson nanoliquid containing microorganisms in a non-Darcy porous medium over a stretching surface under an inclined magnetic field. To tackle this problem, the Bivariate Spectral Quasi Linearization Method (BSQLM) is employed. This method, established by Motsa [23], is selected due to the sensitivity of the model and numerical simplicity. Using univariate functions, this method linearizes the equations, then decouples the system into an independent linearized system. It has been proven to be a sophisticated numerical technique, requiring few grid points to achieve extremely convergent and accurate solutions (Otegbeye and Motsa [24]). Studies like [25–29] made use of the Chebyshev spectral collocation method to study mixed convective flow near a wedge/cone, integrating different aspects of the flow characteristics. This study examines the impact of various flow parameters, such as magnetic parameter, Peclet number, Prandtl number, bio-convective Lewis number, Brownian motion parameter, thermophoresis parameter, and Biot numbers, on flow, energy, nanoparticle accumulation, and the motile microbe density through graphical representations of the numerical solutions. The accuracy of these solutions is verified by evaluating the solution and residual error norms.

2 Mathematical formulation of the problem

Unsteady Casson nanofluid flow with gyrotactic microorganisms in porous medium across a stretching surface is examined using convective boundary conditions and an inclined magnetic field. The plate is extended horizontally, i.e., along χ_1-axis, whereas the χ_2-axis is regarded normal to the plate. A magnetic field of strength B is applied in a direction extending an angle α with the boundary surface. $\alpha = 0$ represents an aligned magnetic field and $\alpha = \frac{\pi}{2}$ represents a transverse magnetic field. At the boundary surface, T_{ss}, C_{ss}, and N_{ss} are the unknown function

values (temperature, nanoparticle concentration, and microbe density, respectively). Eqs. (1) to (5) show the mathematical representation of flow system.

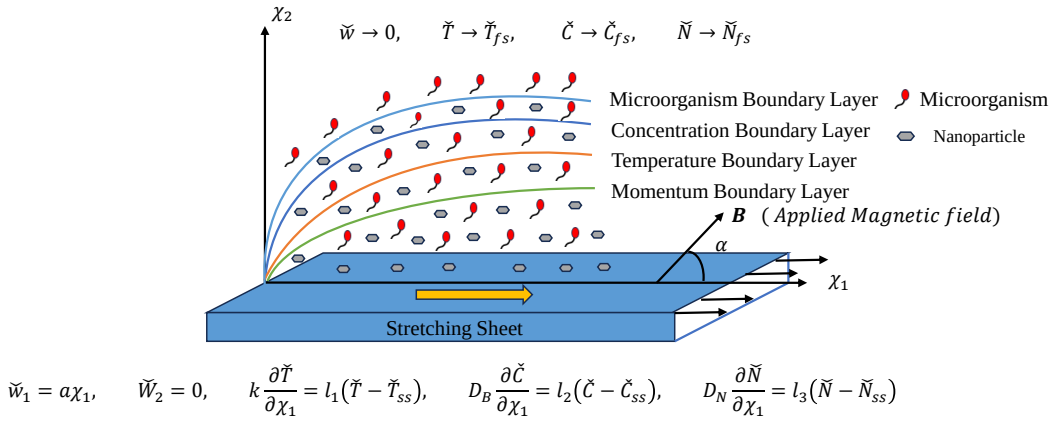

Figure 1. Schematic diagram of flow system

$$\frac{\partial \breve{w}_1}{\partial \chi_1} + \frac{\partial \breve{w}_2}{\partial \chi_2} = 0, \tag{1}$$

$$\frac{\partial \breve{w}_1}{\partial t} + \breve{w}_1\frac{\partial \breve{w}_1}{\partial \chi_1} + \breve{w}_2\frac{\partial \breve{w}_1}{\partial \chi_2} = \nu\epsilon\frac{\partial^2 \breve{w}_1}{\partial \chi_2^2} - \frac{\sigma B^2}{\rho}\sin^2(\alpha)\,\breve{w}_1 - \frac{\nu \breve{w}_1}{k_1} - p^* e^2 \breve{w}_1^2, \tag{2}$$

$$\frac{\partial \breve{T}}{\partial t} + \breve{w}_1\frac{\partial \breve{T}}{\partial \chi_1} + \breve{w}_2\frac{\partial \breve{T}}{\partial \chi_2} = \alpha\frac{\partial^2 \breve{T}}{\partial \chi_2^2} + \tau\left[D_B\frac{\partial \breve{C}}{\partial \chi_2}\frac{\partial \breve{T}}{\partial \chi_2} + \frac{D_{\breve{T}}}{\breve{T}_{fs}}\left(\frac{\partial \breve{T}}{\partial \chi_2}\right)^2\right] + \frac{\sigma}{\rho c_p}B^2 sin^2(\alpha)\breve{w}_1^2, \tag{3}$$

$$\frac{\partial \breve{C}}{\partial t} + \breve{w}_1\frac{\partial \breve{C}}{\partial \chi_1} + \breve{w}_2\frac{\partial \breve{C}}{\partial \chi_2} = D_B\frac{\partial^2 \breve{C}}{\partial \chi_2^2} + \frac{D_{\breve{T}}}{\breve{T}_{fs}}\frac{\partial^2 \breve{T}}{\partial \chi_2^2}, \tag{4}$$

$$\frac{\partial \breve{N}}{\partial t} + \breve{w}_1\frac{\partial \breve{N}}{\partial \chi_1} + \breve{w}_2\frac{\partial \breve{N}}{\partial \chi_2} = D_n\frac{\partial^2 \breve{N}}{\partial \chi_2^2} - \frac{bw_c}{C_{ss} - C_{fs}}\left(\frac{\partial \breve{N}}{\partial \chi_2}\frac{\partial \breve{C}}{\partial \chi_2} + \breve{N}\frac{\partial^2 \breve{C}}{\partial \chi_2^2}\right). \tag{5}$$

Associated boundary conditions are:

$$t = 0 : \forall\, \chi_2;\ \breve{w}_1 = 0, \breve{T} = 0, \breve{C} = 0, \breve{N} = 0, \tag{6}$$

$$\left.\begin{aligned} \breve{w}_1 = a\chi_1,\ K\frac{\partial \breve{T}}{\partial \chi_2} &= l_1(\breve{T}-\breve{T}_{ss}) \\ D_B\frac{\partial \breve{C}}{\partial \chi_2} &= l_2(\breve{C}-\breve{C}_{ss}) \\ D_n\frac{\partial \breve{N}}{\partial \chi_2} &= l_3(\breve{N}-\breve{N}_{ss}) \end{aligned}\right\},\ for\ t>0,\ \chi_2=0, \tag{7}$$

$$\breve{w}_1 \to 0,\ \breve{T}\to \breve{T}_{fs},\ \breve{C}\to \breve{C}_{fs},\ \ N\to \breve{N}_{fs},\ when\ \chi_2\to\infty. \tag{8}$$

We consider the dimensionless variables as:

$$\begin{aligned} &\eta=\chi_2\sqrt{\frac{a}{\nu\chi}},\ \chi=1-e^{-\tau},\ \ \tau=at,\ \ \psi=\chi_1\sqrt{av\chi}f(\eta,\chi), \\ &\chi_1=\frac{\partial\psi}{\partial\chi_2},\ \ \chi_2=-\frac{\partial\psi}{\partial\chi_1},\ \ g(\eta,\chi)=\frac{\breve{T}-\breve{T}_{fs}}{\breve{T}_{ss}-\breve{T}_{fs}},\ h(\eta,\chi)=\frac{\breve{C}-\breve{C}_{fs}}{\breve{C}_{ss}-\breve{C}_{fs}},\ I(\eta,\chi)=\frac{\breve{N}-\breve{N}_{fs}}{\breve{N}_{ss}-\breve{N}_{fs}}. \end{aligned} \tag{9}$$

Using Eq. (9) into Eqs. (1)-(5), we obtain the non-dimensionalised system as:

$$\left(1+\frac{1}{\beta}\right)f'''+\left(\frac{\eta}{2}(1-\chi)+\chi f\right)f''-\chi(1+\Gamma)(f')^2-\chi(1-\chi)\frac{\partial f'}{\partial\chi}-\chi\left(MSin^2(\alpha)+\frac{1}{\delta}\right)f'=0, \tag{10}$$

$$\frac{1}{Pr}g''+\left(\frac{\eta}{2}(1-\chi)+\chi f+Nbh'+Ntg'\right)g'-\chi(1-\chi)\frac{\partial g}{\partial\chi}+\chi EcMSin^2(\alpha)(f')^2=0, \tag{11}$$

$$h''+Le\left(\frac{\eta}{2}(1-\chi)+\chi f\right)h'-Le\chi(1-\chi)\frac{\partial h}{\partial\chi}+\frac{Nt}{Nb}g''=0, \tag{12}$$

$$I''+\left(Lb\chi f-Peh'+\frac{\eta}{2}Lb(1-\chi)\right)I'-Peh''I=Lb\chi(1-\chi)\frac{\partial I}{\partial\chi}+Pe\Omega h''. \tag{13}$$

And the boundary conditions become:

$$f'=0,\ \frac{\partial g}{\partial\eta}=-B_{i_1}\sqrt{\chi}(1-g),\ \frac{\partial h}{\partial\eta}=-B_{i_2}\sqrt{\chi}(1-h),\ \frac{\partial I}{\partial\eta}=-B_{i_3}\sqrt{1-I},\ at\ \eta=0, \tag{14}$$

$$f'\to 0,\ \ g\to 0,\ \ h\to 0,\ \ I\to 0\ \ as\ \eta\to\infty, \tag{15}$$

where the governing parameters are

$$Pr\ =\ \frac{\nu}{\alpha},\ Ec=\frac{a^2x^2}{c_p(\breve{T}_{ss}-\breve{T}_{fs})},\ Nb=\frac{\tau D_B(\breve{C}_{ss}-\breve{C}_{fs})}{\nu},\ Nt=\frac{\tau D_{\breve{T}}(\breve{T}_{ss}-\breve{T}_{fs})}{\breve{T}_{fs}\nu}, \tag{16}$$

$$\delta = \frac{ak_1}{\nu},\ Le = \frac{\nu}{D_B},\ Lb = \frac{\nu}{D_N},\ M = \frac{\sigma B^2 \nu}{\rho w_0^2},\ Pe = \frac{bw_c}{D_N},\ \Omega = \frac{\check{N}_{fs}}{\check{N}_{ss} - \check{N}_{fs}},$$

where Pr, Le, Lb, Pe , ω, N_b, N_t, B_i where $(i = 1, 2, 3)$ are Prandtl number, Lewis number, bio-convective lewis number, Peclet number, microorganism concentration difference parameter, Brownian motion parameter, thermophoresis parameter and the Biot numbers respectively.

3 Solution technique

Given that the Eqs. (10)–(13) are coupled and nonlinear; finding an analytical solution is generally challenging. To address this, we will employ the BSQLM method to numerically solve the system (10)–(13) under the specified boundary conditions (14)-(15). Initially, we assume the system comprises separate equations for f', g, h and I to facilitate solving the equations. To linearize the equations, a quasilinearization approach utilizing Taylor series expansion is applied, as the approximate solutions for each function and their derivatives at the $(r+1)^{\text{th}}$ and r^{th} iteration levels exhibit minor differences. The linearized equations are subsequently solved employing the Chebyshev spectral collocation technique. The nonlinear terms in Eqs. (10)–(13) are handled through this approach. Details of the method can be found in the paper by Trivedi and Ansari [30].
First, we convert Eqs. (10)-(13) into quasilinear form as follows:

$$[a_{0,r}]\, f'''_{r+1} + [a_{1,r}]\, f''_{r+1} + [a_{2,r}]\, f'_{r+1} + [a_{3,r}]\, f_{r+1} = \chi(1-\chi)\frac{\partial f'_{r+1}}{\partial \chi} + a_{4,r}, \tag{17}$$

$$\frac{1}{Pr} g''_{r+1} + [b_{1,r}]\, g'_{r+1} = \chi(1-\chi)\frac{\partial g_{r+1}}{\partial \chi} + b_{2,r}, \tag{18}$$

$$h''_{r+1} + [c_{1,r}]\, h'_{r+1} = Le\chi(1-\chi)\frac{\partial h_{r+1}}{\partial \chi}, \tag{19}$$

$$I''_{r+1} + [e_{1,r}]\, I'_{r+1} + [e_{2,r}]\, I_{r+1} = Lb\chi(1-\chi)\frac{\partial I_{r+1}}{\partial \chi} + e_{3,r}, \tag{20}$$

where the subscripts r and $r+1$ symbolize the iteration levels for the current and prior iterations, respectively.

$$a_{0,r} = \left(1 + \frac{1}{\beta}\right), \quad a_{1,r} = \frac{\eta}{2}(1-\chi) + \chi f_r, \quad a_{2,r} = -2\chi(1+\Gamma) f'_r - \chi\left(M\sin^2(\alpha) + \frac{1}{\delta}\right),$$
$$a_{3,r} = \chi f''_r, \quad a_{4,r} = \chi\left(f_r f''_r - (1+\Gamma) f'^2_r\right), \quad b_{1,r} = \frac{\eta}{2}(1-\chi) + \chi f_{r+1} + Nbh'_r + 2Nt g'_r,$$
$$b_{2,r} = Nt g'^2_r - \chi EcM\sin^2(\alpha) f'^2_{r+1}, \quad c_{1,r} = Le\left(\frac{\eta}{2}(1-\chi) + \chi f_{r+1}\right),$$
$$e_{1,r} = Lb\chi f_{r+1} - Peh'_{r+1} + \frac{\eta}{2}Lb(1-\chi), \quad e_{2,r} = -Peh''_{r+1}, \quad e_{3,r} = Pe\Omega h''_{r+1}.$$

The time and space domains are mapped to $[-1, 1]$ employing a linear transformation to execute the Chebyshev collocation spectral technique on the system (17)-(20). The interval $[-1, 1]$ is discretized using Gauss-Lobatto points (x_i, t_j), where $i = 0, 1, 2, 3, \ldots, N_\eta$ and $j = 0, 1, 2, 3, \ldots, N_\chi$, with N_η and N_χ representing the number of grid points in the spatial and temporal directions,

respectively.

$$x_i = \cos\left(\frac{\pi i}{N_\eta}\right), \quad t_j = \cos\left(\frac{\pi j}{N_\chi}\right).$$

In this context, x and t represent the discretization points for space and time, respectively, with N_η and N_χ denoting the number of chosen collocation points for spatial and temporal domains. To approximate the functions f', g, h, and I, Lagrange polynomials are utilized as the basis functions. The derivatives of these basis functions are used to form a coefficient matrix that approximates the function derivatives. This matrix is known as the differentiation matrix, commonly represented by $\mathbf{D}$ in the spatial domain and $\mathbf{d}$ in the temporal domain. Employing Chebyshev spectral collocation on Eqs. (17)-(20) results in the derived scheme.

$$\left((a_{0,r})\,\mathbf{D}^3 + [\mathbf{a}_{1,r,i}]\,\mathbf{D}^2 + [\mathbf{a}_{2,r,i}]\,\mathbf{D} + [\mathbf{a}_{3,r,i}]\right)\mathbf{F}_{r+1,i} - \chi(1-\chi)\sum_{j=0}^{N_\chi-1}\mathbf{d}_{i,j}\mathbf{D}\mathbf{F}_{r+1,j}$$
$$= \chi(1-\chi)\,\mathbf{d}_{i,N_\chi}\mathbf{D}\mathbf{F}_{r+1,N_\chi} + \mathbf{a}_{4,r,i}, \tag{21}$$

$$\left(\frac{1}{Pr}\mathbf{D}^2 + [\mathbf{b}_{1,r,i}]\,\mathbf{D}\right)G_{r+1,i} - \chi(1-\chi)\sum_{j=0}^{N_\chi-1}\mathbf{d}_{i,j}\mathbf{I}\mathbf{G}_{r+1,j} = \chi(1-\chi)\,\mathbf{d}_{i,N_\chi}\mathbf{G}_{r+1,N_\chi} + \mathbf{b}_{2,r,i}, \tag{22}$$

$$\left(\mathbf{D}^2 + [\mathbf{c}_{1,r,i}]\,\mathbf{D}\right)\mathbf{G}_{r+1,i} - \chi(1-\chi)\sum_{j=0}^{N_\chi-1}\mathbf{d}_{i,j}\mathbf{I}\mathbf{H}_{r+1,j} = \chi(1-\chi)\,\mathbf{d}_{i,N_\chi}\mathbf{H}_{r+1,N_\chi} + \mathbf{c}_{2,r,i}, \tag{23}$$

$$\left(\mathbf{D}^2 + [\mathbf{e}_{1,r,i}]\,\mathbf{D} + [\mathbf{e}_{2,r,i}]\right)\mathbf{\Phi}_{r+1,i} - \chi(1-\chi)\sum_{j=0}^{N_\chi-1}\mathbf{d}_{i,j}\mathbf{I}\mathbf{\Phi}_{r+1,j} = \chi(1-\chi)\,\mathbf{d}_{i,N_\chi}\mathbf{\Phi}_{r+1,N_\chi} + \mathbf{e}_{3,r,i}, \tag{24}$$

where $\mathbf{I}$ is $(N_\eta+1)\times(N_\eta+1)$ sized identity matrix. The corresponding boundary conditions become

$$\begin{aligned}
&\mathbf{D}_{0,j}\mathbf{F}_{r+1,i} = 0, \quad \mathbf{D}_{N_\eta,j}\mathbf{F}_{r+1,i} = 1, \quad \mathbf{I}_{N_\eta,j}\mathbf{F}_{r+1,i} = 0,\\
&\mathbf{D}_{0,j}\mathbf{G}_{r+1,i} - Bi_1\sqrt{\chi}\mathbf{I}_{0,j}\mathbf{G}_{r+1,i} = -Bi_1\sqrt{\chi}, \quad \mathbf{I}_{N_\eta,j}\mathbf{G}_{r+1,j} = 0,\\
&\mathbf{D}_{0,j}\mathbf{H}_{r+1,i} - Bi_2\sqrt{\chi}\mathbf{I}_{0,j}\mathbf{H}_{r+1,i} = -Bi_2\sqrt{\chi}, \quad \mathbf{I}_{N_\eta,j}\mathbf{H}_{r+1,j} = 0,\\
&\mathbf{D}_{0,j}\mathbf{\Phi}_{r+1,i} - Bi_3\sqrt{\chi}\mathbf{I}_{0,j}\mathbf{\Phi}_{r+1,i} = -Bi_3\sqrt{\chi}, \quad \mathbf{I}_{N_\eta,j}\mathbf{\Phi}_{r+1,j} = 0,
\end{aligned}$$

The solution of Eqs. (10) to (15) obtained by taking $\xi = 1$, is considered as initial solution for this numerical scheme.

4 Convergence and accuracy

Convergence

By calculating the difference in solutions at the end of each iteration, we evaluate the convergence of BSQLM. We argue that our method converges when the difference between solutions gets small enough that there is no effect from increasing the number of iterations. The solution error norms are produced thus;

$$\| f' \|_\infty = \max_{0 \le i \le M_x} \| f'_{r+1,i} - f'_{r,i} \|_\infty, \tag{25}$$

$$\| g \|_\infty = \max_{0 \le i \le M_x} \| g_{r+1,i} - g_{r,i} \|_\infty, \tag{26}$$

$$\| h \|_\infty = \max_{0 \le i \le M_x} \| h_{r+1,i} - h_{r,i} \|_\infty, \tag{27}$$

$$\| I \|_\infty = \max_{0 \le i \le M_x} \| I_{r+1,i} - I_{r,i} \|_\infty. \tag{28}$$

Solution error norms

Between two consecutive replications, the solution error norms are calculated by considering $M = 3$, $\alpha = \pi/6$, $\delta = 0.2$,$Le = 15$, $Nb = 0.2$, $Nt = 0.005$, $Ec = 0.05$, $Pr = 12$, $Lb = 1$, $Pe = 0.1$, $B_{i_1} = 0.05$, $B_{i_2} = 0.2$, $B_{i_3} = 0.02$ and $\Omega = 0.5$. We call this error a solution-based error.

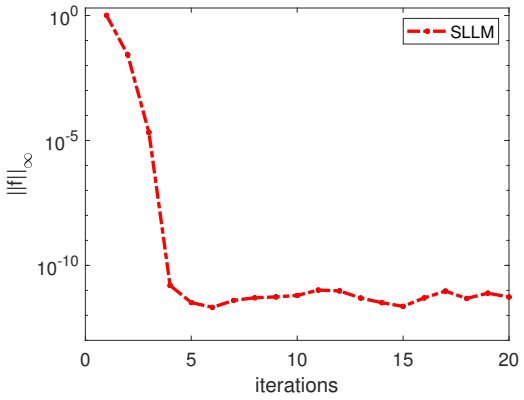

Figure 2. Solution error of f' with iteration

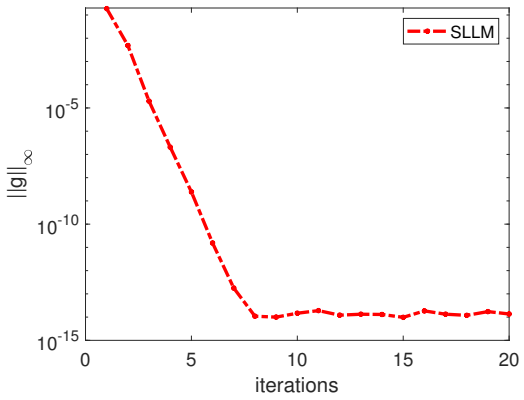

Figure 3. Solution error of g with iteration

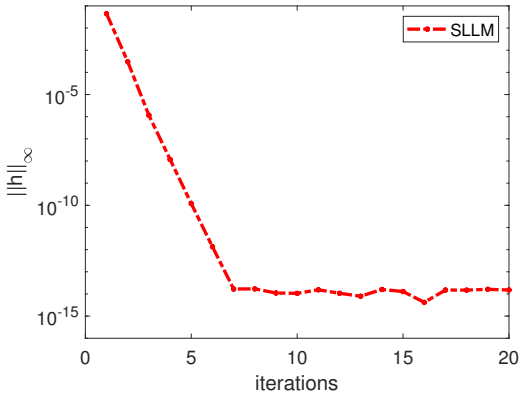

Figure 4. Solution error of h with iteration

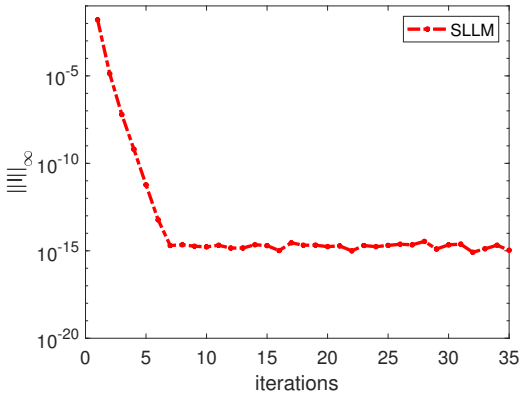

Figure 5. Solution error of I with iteration

Figure 2, Figure 3, Figure 4 and Figure 5 show the solution error norms for f', g, h, and I, respectively. In this case, the absolute value error is reduced to a tolerance value of 10^{-12} in 5 iterations for f'. For g, it took 8 iterations to reduce the error to the tolerance level of 10^{-14}. For h and I it took almost 6 iterations to reduce the error to 10^{-14} as a result, the iteration strategy has acquired good convergence.

Accuracy

We compute the residual error by deploying the approximate solutions generated in place of the original system of equations in order to evaluate the accuracy of BSQLM. This illustrates how near our solution is to the analytical true solutions of the differential equation system. We define the norms for residual errors as:

$$\begin{aligned} \boldsymbol{Res(f)} = \max_{0\le i\le M_x} \Bigg|\Bigg| &\left(1+\frac{1}{\beta}\right) f''' + [0.5\eta(1-\chi)+\chi f']f'' \\ &-\chi(1+\Gamma)(f')^2 - \chi(1-\chi)\frac{\partial^2 f}{\partial\chi\partial\eta} - \chi\left(MSin^2(\alpha)+\frac{1}{\delta}\right) f' \Bigg|\Bigg|_\infty , \end{aligned} \tag{29}$$

$$\begin{aligned} \boldsymbol{Res(g)} = \max_{0\le i\le M_x} \Bigg|\Bigg| &\frac{1}{Pr} g'' + [0.5\eta(1-\chi)+\chi f + Nbh' + Ntg']g' \\ &-\chi(1-\chi)\frac{\partial g}{\partial\chi} + \chi EcMSin^2(\alpha)(f')^2 \Bigg|\Bigg|_\infty , \end{aligned} \tag{30}$$

$$\boldsymbol{Res(h)} = \max_{0\le i\le M_x} \left|\left| h'' + Le(0.5\eta(1-\chi)+\chi f)h' - Le\chi(1-\chi)\frac{\partial h}{\partial\chi} + \frac{Nt}{Nb}g'' \right|\right|_\infty , \tag{31}$$

$$\begin{aligned} \boldsymbol{Res(I)} = \max_{0\le i\le M_x} \Bigg|\Bigg| &I'' + [Lb\chi f - Peh'' + \frac{1}{2}Lb(1-\chi\eta)]I' - Peh''I \\ &- Lb\chi(1-\chi)\frac{\partial I}{\partial\chi} - Pe\Omega h'' \Bigg|\Bigg|_\infty . \end{aligned} \tag{32}$$

Residual error norms

Figure 6, Figure 7, Figure 8 and Figure 9 display the closeness of the obtained solution to the true solution, determining the residual norms of the solutions for f', g, h, and I, respectively. The residual error of the PDEs (10)-(13) is estimated by using the values $M = 3$, $\alpha = \pi/6$, $\delta = 0.2$, $Le = 15$, $Pr = 10$, $Nb = 0.2$, $Nt = 0.005$, $Ec = 0.05$, $Lb = 1$, $Pe = 0.1$, $B_{i_1} = 0.05$, $B_{i_2} = 0.2$, $B_{i_3} = 0.02$, and $\Omega = 0.5$. The residual error is calculated by taking the maximum infinite norm of the values obtained by replacing the approximate solutions from the preferred numerical technique into the original system (10)-(13). This error measures how close the numerical solutions are to the analytical solutions of the system. Notably, an accuracy of nearly 10^{-9} is achieved for f' in just a few iterations, and for g, the error is reduced to 10^{-15} after five iterations. For h, the error decreases to 10^{-14} after a few iterations, and for I, the error reaches 10^{-14} after two iterations.

Figure 10, Figure 11, Figure 12 and Figure 13 illustrate that the residual errors of the resulting numerical solutions for f', g, h, and I converge to accuracies of 10^{-10}, 10^{-15}, 10^{-14}, and 10^{-14}, respectively, after the first iteration in the time domain.

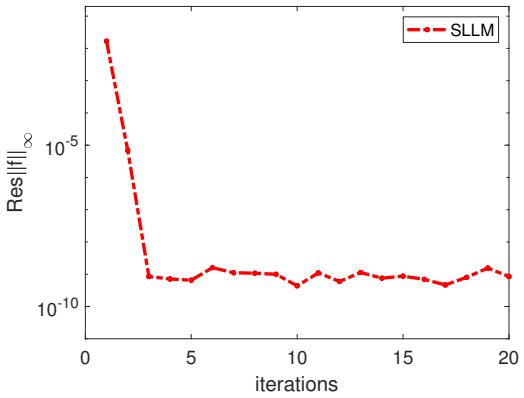

Figure 6. Residual error of f' with iteration

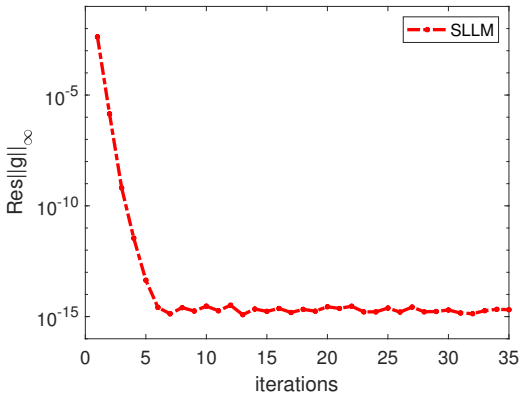

Figure 7. Residual error of g with iteration

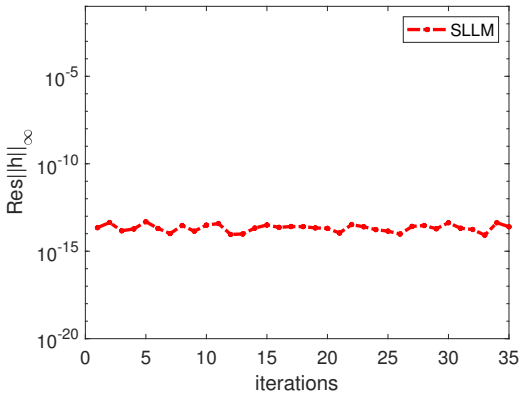

Figure 8. Residual error of h with iteration

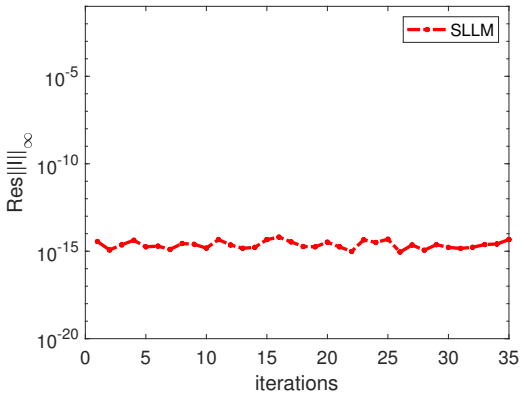

Figure 9. Residual error of I with iteration

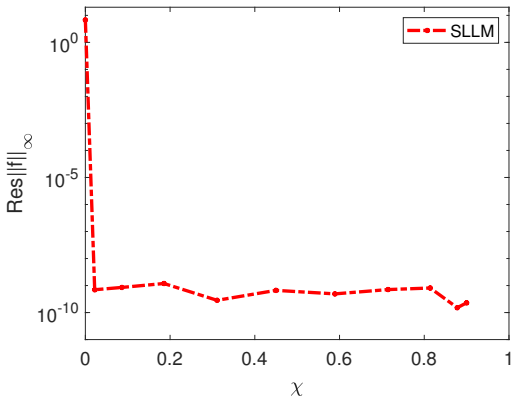

Figure 10. Residual error behaviour of f' with χ

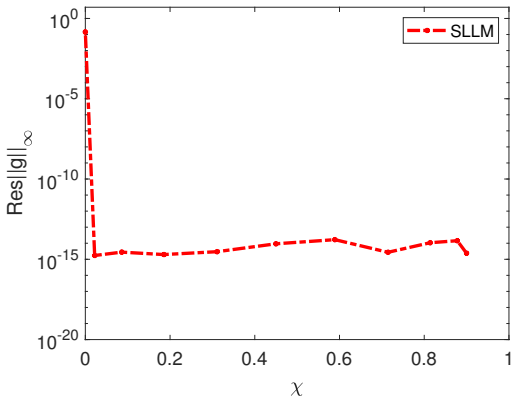

Figure 11. Residual error behaviour of g with χ

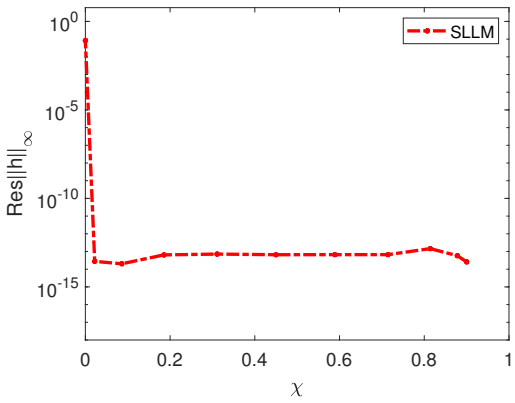

Figure 12. Residual error behaviour of h with χ

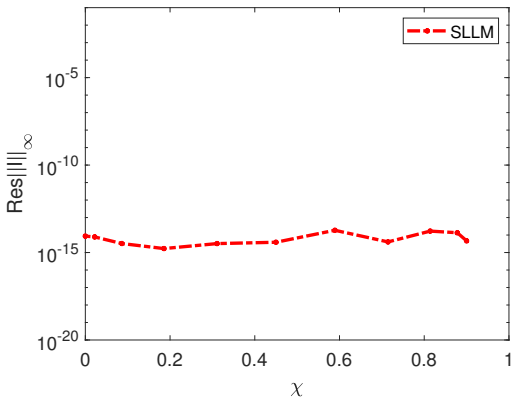

Figure 13. Residual error behaviour of I with χ

5 Results and discussion

The BSQLM derived numerical solutions to governing differential equations, which are shown in tabular and graphical form. To investigate heat and flow behavior, a brief review of the relevant physics to the impact of important flow parameters on a dimensional velocity $f^{'}$, gyrotactic microbe density I, temperature g, and nanoparticle concentration h is provided. Figures were created by taking the parametric values into account as $M = 3$, $\alpha = \pi/24$, $\delta = 0.2$, $Nb = 0.2$, $Nt = 0.05$, $Le = 5$, $Ec = 0.2$, $Lb = 1$, $Pr = 10$, $Pe = 0.1$, $B_{i_1} = 0.05$, $B_{i_2} = 0.01$, $B_{i_3} = 0.01$, $\Omega = 1$, $\Gamma = 0.2$. These values are in agreement with the literature.

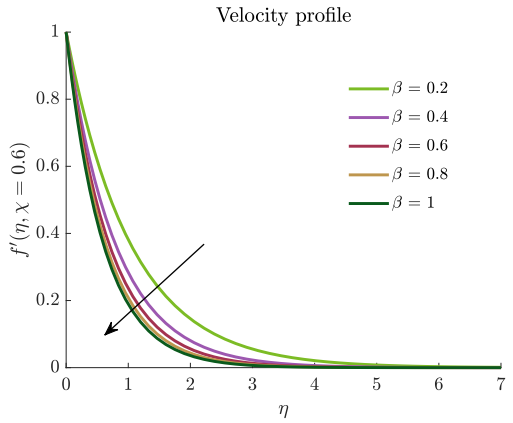

Figure 14. Impact of β on velocity

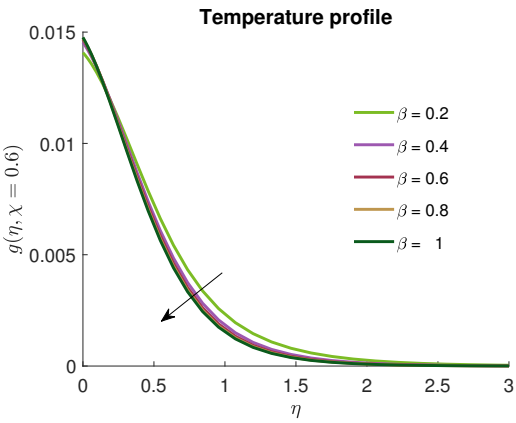

Figure 15. Impact of β on temperature

Influence of β on $f^{'}$ and g

Figure 14 and Figure 15 show how Casson parameter β impacts velocity and temperature patterns. Amplification in β improves the viscosity of the fluid. Fluid undergoes a shear-thickening process as β increments, reducing fluidity and the width of the momentum boundary layer. Figure 15 shows a noticeable rise in nanofluid temperature due to the elevated value of β. An excellent agreement occurs with these observations and the results reported by [30–33].

Impact of α on g, h and I

Figure 16 and Figure 17 presents the influence of varying α on velocity and heat transfer field. The greater value of α strengthens the electromagnetic contact, leads to impeded flow, and aids in

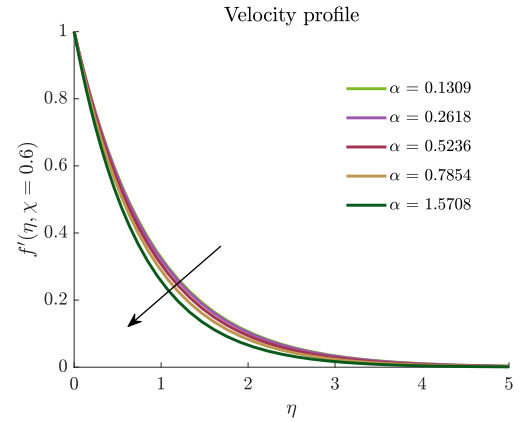

Figure 16. Effect of α on velocity

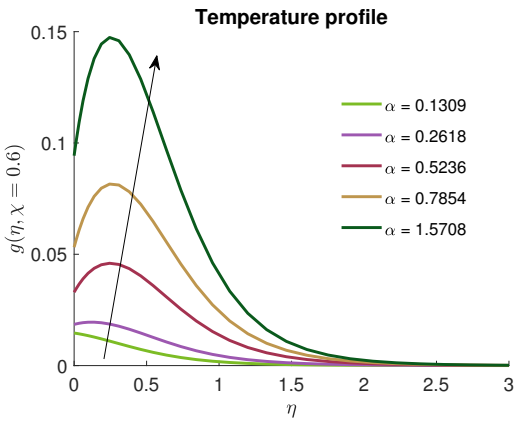

Figure 17. Effect of α on temperature

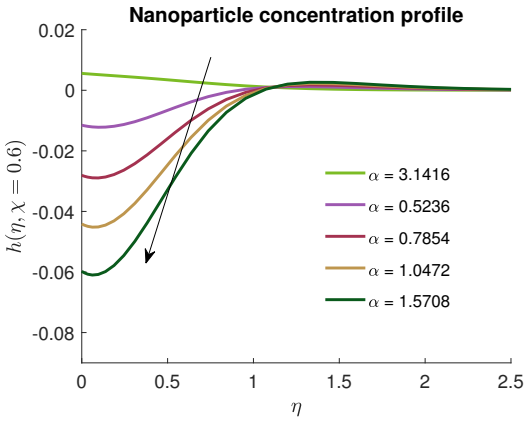

Figure 18. Impact of α on nanoparticle concentration

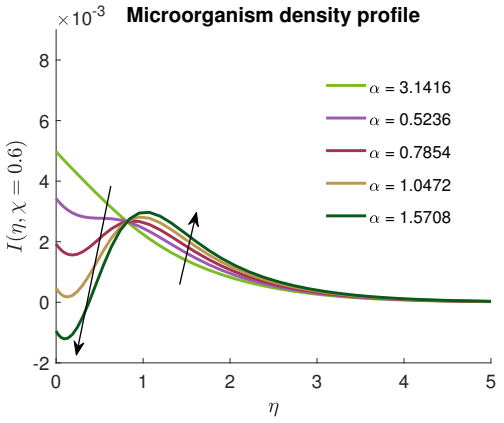

Figure 19. Impact of α on microorganism density

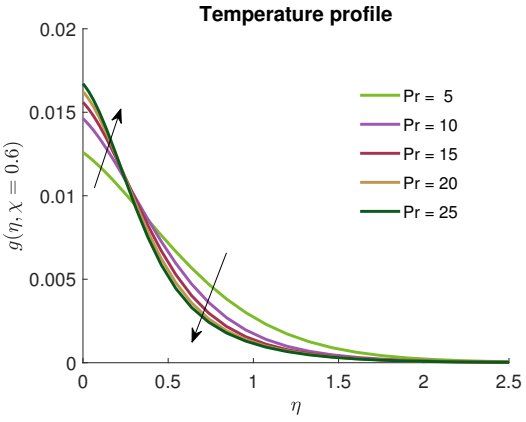

Figure 20. Effect of Pr on temperature

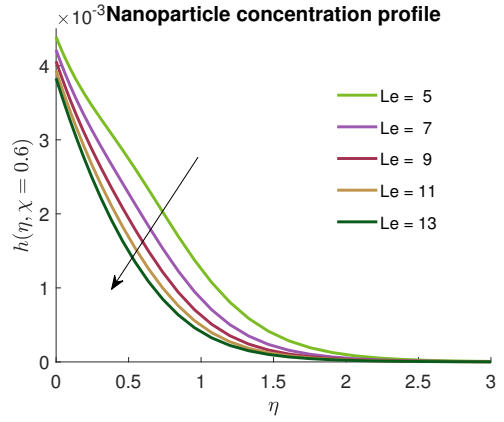

Figure 21. Impact of Le on nanoparticle concentartion

the retention of heat in the boundary layer region. The temperature distribution improves as the inclination angle goes up, and the thermal boundary thins. Figure 18 describes the variation in the nanoparticle concentration field against the angle of inclination. This figure illustrates that the nanoparticle concentration diminishes in response to the growing values of inclination angle, and this phenomenon is advocated by the movement of nanoparticles from the fluid towards the plate. Figure 19 depicts the behavior of the microorganism density profile with the varying values of α. It has been observed that the microbe density drops down near the surface, as the microorganisms

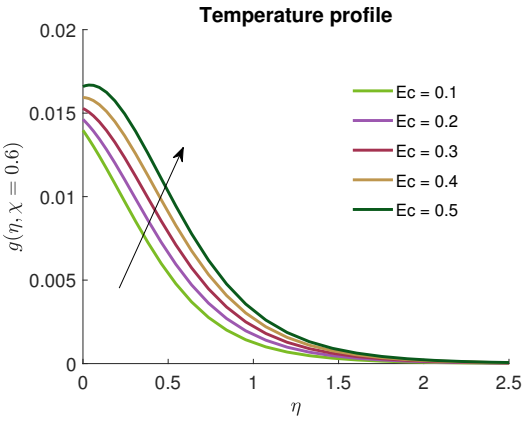

Figure 22. Variation in temperature for varying values of Ec

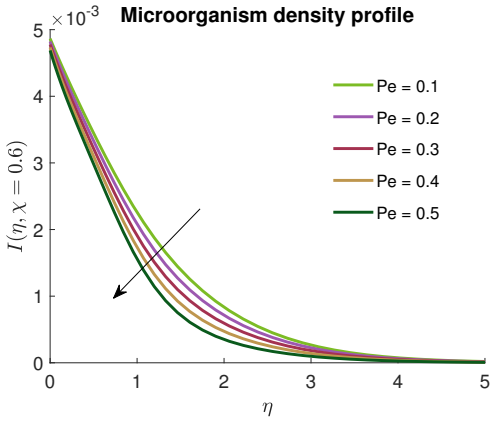

Figure 23. Impact of Pe on microbe density

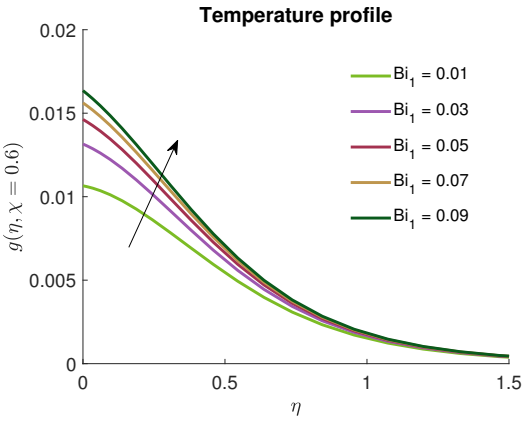

Figure 24. Impact of Bi_1 on temperature

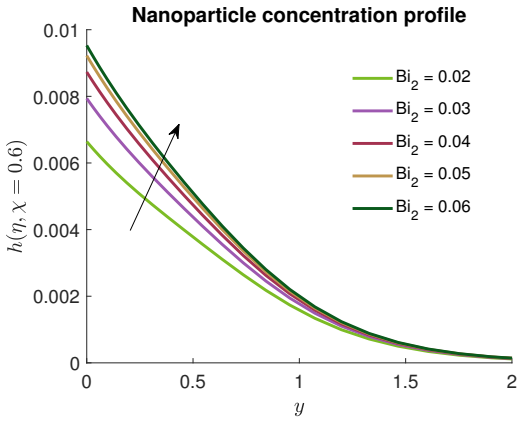

Figure 25. Effect of Bi_2 on nanoparticle concentration

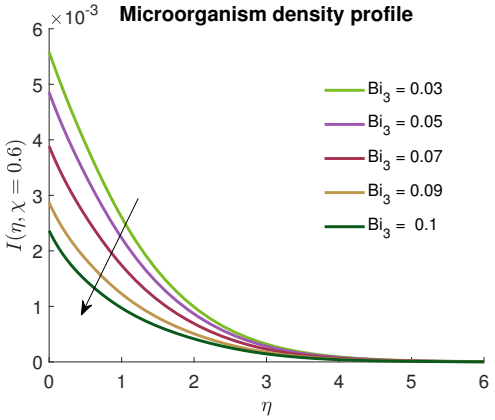

Figure 26. Impact of Bi_3 on microbe density

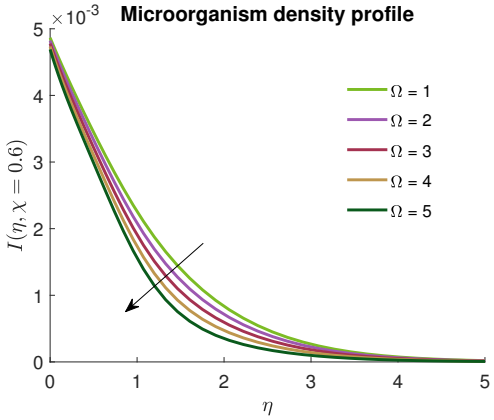

Figure 27. Impact of Ω on microbe density

move towards the plate due to the Lorentz force effect and away from the wall microbe density improves till it reaches the free stream condition. The present findings are substantiated by the studies, namely [20, 34].

Impact of Pr on temperature field g

From Figure 20, the temperature distribution notably shows a two-fold nature as the Prandtl number gets larger values. Generally, fluid physics says that, increment in Pr drops down the

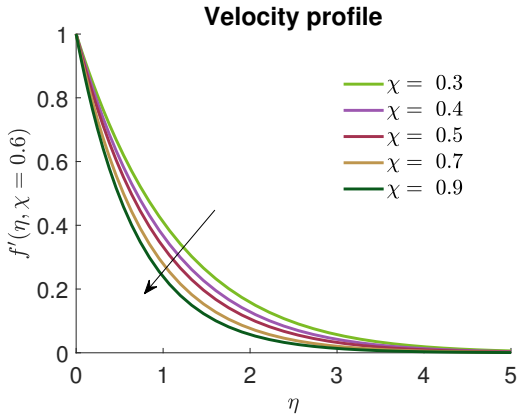

Figure 28. Impact of time on velocity profile

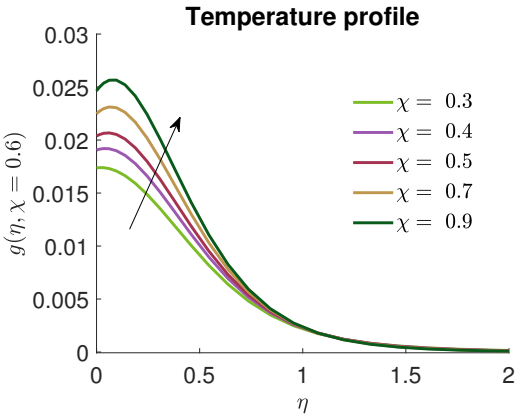

Figure 29. Impact of χ on temperature

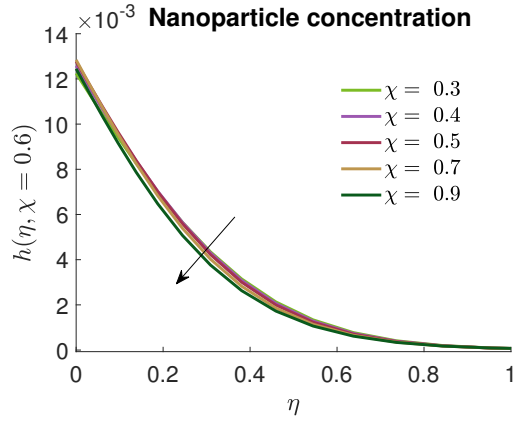

Figure 30. Nanoparticle concentration in response to time

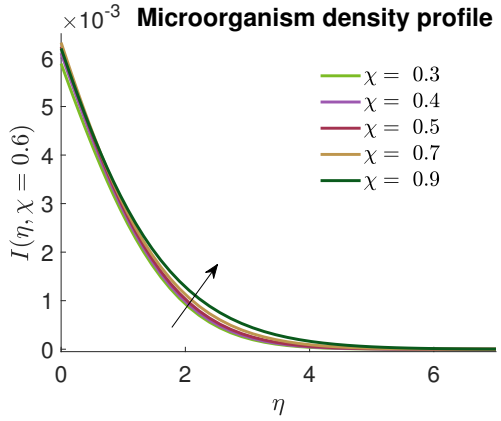

Figure 31. Impact on microbe density for varying time

thermal diffusivity, which restricts the heat from diffusing into the fluid bulk and thereby it rises the fluid temperature near the wall. The incorporation of the convective boundary condition and strong Lorentz force near the surface also plays its role in advocating this observation. Consequently, the thermal boundary layer becomes thinner and the temperature drops uniformly and more steeply as the distance from the wall increases. Our observations hold good agreement with the results documented by [32, 35, 36].

Impact on nanoparticle concentration(h) due to changing values of Le and Ec

The Lewis number establishes a connection between the mass diffusivity and thermal conductivity of the nanofluid. Figure 21 explains the impact of the Lewis number on the concentration distribution field. As the Lewis number rises, the concentration distribution improves. The concentration distribution improves due to the reduction in mass diffusivity relative to thermal diffusivity, resulting in a thinner concentration boundary layer and a steeper concentration gradient near the surface. This enhances the mass transfer rate from the stretching surface into the fluid. Figure 22 displays the observation that the parameter Ec shows a comparable inverse correlation with the temperature distribution due to the enhancement of viscous dissipation effects. This phenomenon leads to a conversion of kinetic energy into internal energy, thereby raising the temperature in the fluid and thickening the thermal boundary layer. These observations are in good agreement with those of Joshi [35, 37–39].

Impact on microorganism density (I) due to changing values of Pe

Figure 23 illustrates effect of the Peclet number $(\boldsymbol{Pe})$ on the microorganism distribution profile $\chi(\eta)$. The result reveals that growing values of $\boldsymbol{Pe}$ lead to a reduction in the microorganism concentration profile. An increase in the Peclet number, which represents the ratio of advection to diffusion rates for microorganisms, enhances the convective transport of microbes along the flow direction, thereby decreasing their local concentration. In fluid systems, the Peclet number is typically associated with heat transfer processes, indicating the relative strength of convection over diffusion. Consequently, higher Peclet numbers alter the distribution pattern of $\chi(\eta)$, as greater advection rates accelerate microorganism swimming, reducing their accumulation within the boundary layer. This observation holds good agreement with that of [35, 39].

Consequence of biot numbers Bi_1, Bi_2 and Bi_3 on g, h and I, respectively

Figure 24 displays the behavior of the temperature field in response to rising thermal biot number $\boldsymbol{Bi_1}$. An improving pattern in the temperature field is observed in response to an upsurge in thermal Biot number. In terms of physics, the enhanced thermal biot parameter results in a decrease in the resistance to the flow by increasing the intermolecular movement, which raises the temperature gradient close to the surface. This physical confirmation leads to an increase in the temperature distribution near the surface. Figure 25 set forth the influence on the concentration profile by the elevated solutal Biot number. It is demonstrated by the figure that the $\boldsymbol{Bi_2}$ enhances the concentration profile. Physically, the biot parameter drags down the opposition to the energy transport from the body, which leads to an upsurge in the concentration gradient near the boundary layer. This physical demonstration states a rise in nanoparticle concentration near the boundary layer. Figure 26 shows how the motile microbe density profile is impacted by the growing microbe biot number. The graphical conclusion demonstrates that with the growing values of $\boldsymbol{Bi_3}$, the microbe density profile drops due to the movement of the microorganisms. Results in the papers like [32, 36, 37, 40, 41] have shown similar observations.

Impact of Ω on microbe density

Figure 27 reports the effects of the microorganism difference parameter on the motile microorganism density profile. It is noteworthy that the density distribution of motile microorganisms exhibits a dropping behavior against the microorganism parameter. Increase in $\boldsymbol{\Omega}$ and convective motion enhances the upward or outward diffusion of microorganisms away from the surface because the microorganism flux tends to move from regions of higher density to lower density. Similar observations were reported by [42, 43].

Impact of time on velocity, temperature, nanoparticle concentration, and microbe density

Figure 28, Figure 29, Figure 30 and Figure 31 give a visual perception of response that the fluid velocity, temperature, nanoparticle concentration and microorganism density show with time. Figure 29, Figure 30 and Figure 31 illustrate how time enhances temperature and microbe density profiles. Specifically, thermal and microbe density boundary layers emerge with time, while momentum and concentration boundary layers diminish with time depicted in Figure 28 and Figure 30. The values of heat transfer coefficient (Nusselt number) and mass transfer coefficient (Sherwood number) are depicted in Table 1 for varying inclination angle of magnetic field, time, Prandtl number, and biot numbers. The nomenclature is displayed in Table 2.

Table 1. Impact of α, χ , Pr, B_{i_1}, B_{i_2} and B_{i_3} on Nusselt number (Nu_x) and Sherwood number (Sh_x)

α	χ	Pr	B_{i_1}	B_{i_2}	B_{i_3}	Nu_x	Sh_x
$\pi/24$	0.7	10	0.05	0.01	0.01	0.006455	0.005402
$\pi/12$						0.021296	0.007420
$\pi/6$						0.119828	0.0146809
$\pi/4$						0.247389	0.023967
$\pi/2$						0.482958	0.041386
	0.3					0.022210	0.016994
	0.4					0.020962	0.033608
	0.5					0.026916	0.018598
	0.7					0.026597	0.033389
	0.9					0.027576	0.035571
		5				0.004440	0.005503
		10				0.006455	0.005402
		15				0.007385	0.005355
		20				0.007918	0.005331
		25				0.008259	0.005317
			0.01			0.002890	0.005761
			0.03			0.005645	0.005531
			0.05			0.006455	0.005402
			0.07			0.006274	0.005322
			0.09			0.005468	0.005270
				0.02		0.006435	0.008214
				0.03		0.006419	0.009886
				0.04		0.006405	0.010954
				0.05		0.006393	0.011667
				0.06		0.006382	0.012152
					0.03	0.006455	0.005402
					0.05	0.006455	0.005402
					0.07	0.006455	0.005402
					0.09	0.006455	0.005402
					1	0.006455	0.005402

Table 2. Nomenclature

$\epsilon : \left(1+\frac{1}{\beta}\right)$	χ : *Dimensionless time*
ν : *Kinematic viscosity* (m^2/s)	B : *Magnetic field*
ρ : *Density* (kg/m^3)	c_p : *Specific heat* (J/kgK)
u : *Velocity of the fluid* (m/s)	α : *Thermal diffusivity* (m^2/s)
D_T : *Thermophoresis diffusivity* (m^2/s)	D_B : *Brownian diffusivity* (m^2/s)
ρc_p : *Heat capacity of nanoparticles* (J/K)	T : *Dimensional temperature* (K)
T_{ss} : *Wall temperature* (K)	C_{ss} : *Wall concentration* (mol/m^3)
N_{ss} : *Wall motile microorganisms* $(microorganisms/m^2)$	N_{nfs} : *Ambient microorganisms*
C : *Dimensional concentration* (mol/m^3)	Pr : *Prandtl number*
T_{nfs} : *Ambient temperature* (K)	N_t : *Thermophoresis number*
N_b : *Brownian motion number*	C_{nfs} : *Ambient concentration* (mol/m^3)
λ_1 : *Ratio relaxation to retardation time*	λ_2 : *The relaxation time* (s)
B_{i_1} : *Thermal Biot number*	B_{i_2} : *Solutal Biot number*
$(\rho c)_p$: *Effective heat capacity of the nanoparticle material*	$(\rho c)_f$: *Heat capacity of the fluid* (J/K)
β : *Casson fluid parameter* (N/m^2)	Le : *Lewis number*
Ec : *Eckert number*	M : *Magnetic parameter*
q' : *Dimensioless velocity*	g : *Dimensionless temperature*
h : *Dimensionless concentration*	B_{i_3} : *Microbe Biot number*
I : *Dimensionless microbe density*	Wc : *Swimming speed ofmicrobes* (m/s)
Lb : *Bioconvection lewis parameter*	Ω : *Microorganism difference parameter*
p^*e^2 : *Non − uniform inertia parameter*	

6 Conclusion

Transient magnetohydrodynamic boundary layer flow of Casson nanofluid containing microorganisms close to an expanding boundary in a non-Darcy porous medium is examined. Effects of inclined magnetic field, Joule dissipation and convective conditions in temperature, concentration of nanoparticles and density of microbes are considered. The partial differential equations, replicating the flow system, are non-dimensionalized and retained in the same form. A numerical procedure, namely, the bivariate spectral quasi-linearization method, is exercised to achieve a solution of high precision of a nonlinear and coupled system of partial differential equations. The convergence and accuracy of the solution method are assessed by computing the solution and residual error norms. Outcomes are also compared with the results available in the literature and found good agreement. Graphical sketches of numerical results are drawn, and variations in flow, heat transfer, nanoparticle, and microbe density are discussed. An extremely careful analysis of results leads to the following outcomes:

- Casson parameter uniformly diminishes the velocity and temperature inside the boundary layer region.
- Angle of inclination (α) boosts the temperature profile near the boundary and decreases the fluid velocity and nanoparticle concentration.
- Prandtl number gives a rise in temperature near the wall and reveals an opposite effect away from the thermal boundary layer region.
- Lewis number exerts a diminishing impact on nanoparticle concentration field.
- Eckert number thickens the thermal boundary layer region.
- Microbe density field is a decreasing function of Peclet number.
- Solutal, thermal, and microorganism biot number exert, respectively, an enhancing effect on nanoparticle concentration, a diminishing influence on temperature profile, and microbe density.

The bioconvection fluid flow problem under consideration is employed in a variety of technological and engineering applications, including heat exchangers, gas turbines, vehicle radiators, microbe fuel cells, reactors for nuclear power, and biomedical applications.

7 Limitations

This study is performed by assuming constant thermophysical properties of the fluid. Radiation, Chemical reaction, activation energy, Soret and Dufor effects, size of nanoparticles, impact of nanoparticles on fluid flow, and induced magnetic field are neglected in this paper. The main limitation of this work is the lack of comparison with experimental work.

8 Future research

To carry out further advancement on this work, one can consider different geometries like a spinning disc, a cone, a cylinder, etc. This study can also be performed by considering variable thermophysical properties and the induced magnetic field.

Declarations

Use of AI tools

The authors declare that they have not used Artificial Intelligence (AI) tools in the creation of this article.

Data availability statement

No Data associated with the manuscript.

Ethical approval (optional)

The authors state that this research complies with ethical standards. This research does not involve either human participants or animals.

Consent for publication

All authors unanimously agreed to publish this article in the Mathematical Modeling and Numerical Simulation with Applications.

Conflicts of interest

The authors declare that they have no conflict of interest.

Funding

No funding was received for this research.

Author's contributions

T.F.: Conceptualization, Methodology. M.S.A.: Writing—review and Editing, Supervision, Validation. O.O.: Data Curation, Resources, Software. M.T.: Writing—original Draft Preparation. All authors have read and agreed to the published version of the manuscript.

Acknowledgements

Not applicable

References

[1] Paulusse, J.M. and Sijbesma, R.P. Molecule-based rheology switching. *Angewandte Chemie International Edition*, 45(15), 2334-2337, (2006). [CrossRef]

[2] Chen, H., Ding, Y. and Tan, C. Rheological behaviour of nanofluids. *New Journal of Physics*, 9, 367, (2007). [CrossRef]

[3] Li, X., Zou, C., Wang, T. and Lei, X. Rheological behavior of ethylene glycol-based SiC nanofluids. *International Journal of Heat and Mass Transfer*, 84, 925-930, (2015). [CrossRef]

[4] Motahari, K., Moghaddam, M.A. and Moradian, M. Experimental investigation and development of new correlation for influences of temperature and concentration on dynamic viscosity of MWCNT-SiO_2 (20-80)/20W50 hybrid nano-lubricant. *Chinese Journal of Chemical Engineering*, 26(1), 152-158, (2018). [CrossRef]

[5] Evangelista, R.R., Sanches, M.A.R., Castilhos, M.B., Cantú-Lozano, D. and Telis-Romero, J. Determination of the rheological behavior and thermophysical properties of malbec grape juice concentrates (*Vitis vinifera*). *Food Research International*, 137, 109431, (2020). [CrossRef]

[6] Sayed-Ahmed, M.E., Attia, H.A. and Ewis, K.M. Time dependent pressure gradient effect on unsteady MHD Couette flow and heat transfer of a Casson fluid. *Engineering*, 3(1), 38-49, (2011). [CrossRef]

[7] Aman, S., Khan, I., Ismail, Z., Salleh, M.Z., Alshomrani, A.S. and Alghamdi, M.S. Magnetic field effect on Poiseuille flow and heat transfer of carbon nanotubes along a vertical channel filled with Casson fluid. *AIP Advances*, 7(1), 015036, (2017). [CrossRef]

[8] Kala, B.S., Rawat, M.S., Rawat, N. and Kumar, A. Numerical analysis of non-Darcy MHD flow of a Carreau fluid over an exponentially stretching/shrinking sheet in a porous medium. *International Journal of Scientific Research in Mathematical and Statistical Sciences*, 6(2), 295-303, (2019). [CrossRef]

[9] Renu, K., Kumar, A., Kumar, A. and Kumar, J. Effect of transverse hydromagnetic and media permeability on mixed convective flow in a channel filled by porous medium. *Special Topics & Reviews in Porous Media: An International Journal*, 12(2), 1-23, (2020). [CrossRef]

[10] Kala, B.S, Rawat, M.S. and Kumar. A. Numerical analysis of the flow of a Casson fluid in magnetic field over an inclined nonlinearly stretching surface with velocity slip in a Forchheimer porous medium. *Asian Research Journal of Mathematics*, 16(7), 34-58. (2020). [CrossRef]

[11] Kuznetsov, A.V. Bio-thermal convection induced by two different species of microorganisms. *International Communications in Heat and Mass Transfer*, 38(5), 548-553, (2011). [CrossRef]

[12] Raju, C.S.K. and Sandeep, N. Heat and mass transfer in MHD non-Newtonian bio-convection flow over a rotating cone/plate with cross diffusion. *Journal of Molecular Liquids*, 215, 115-126, (2016). [CrossRef]

[13] Raju, C.S.K and Sandeep, N. Dual solutions for unsteady heat and mass transfer in bio-convection flow towards a rotating cone/plate in a rotating fluid. *International Journal of Engineering Research in Africa*, 20, 161-176, (2016). [CrossRef]

[14] Ray, A.K., Vasu, B., Anwar Beg, O., Gorla, R.S.R. and Murthy, P.V.S.N. Magneto-bioconvection flow of a Casson thin film with nanoparticles over an unsteady stretching sheet: HAM and GDQ computation. *International Journal of Numerical Methods for Heat & Fluid Flow*, 29(11), 4277-4309, (2019). [CrossRef]

[15] Oyelakin, I.S., Mondal, S. and Sibanda, P. Nonlinear radiation in bioconvective Casson nanofluid flow. *International Journal of Applied and Computational Mathematics*, 5, 124, (2019). [CrossRef]

[16] Saeed, A. and Gul, T. Bioconvection casson nanofluid flow together with Darcy-Forchheimer due to a rotating disk with thermal radiation and arrhenius activation energy. *SN Applied Sciences*, 3, 78, (2021). [CrossRef]

[17] Sanjalee, Sharma, Y.D. and Yadav, O.P. Stability analysis of double diffusive thermo-bioconvection in aerobic-microorganism-suspended Casson nanofluid. *The European Physical Journal Plus*, 137, 700, (2022). [CrossRef]

[18] Khan, W., Khan, W., Hussain, S. and Salah, B. A mathematical model of Casson nanofluid flow over a vertically stretched porous surface along with bioconvection, Joule heating and thermal Robin conditions. *Advances in Mechanical Engineering*, 16(9), (2024). [CrossRef]

[19] Sankari, M.S., Rao, M.E., Khan, W., Makinde, O.D., Chamkha, A.J. and Salah, B. Homotopic analysis for bioconvection of Casson nanofluid flow over an exponential stretching sheet with activation energy and motile microorganism. *Numerical Heat Transfer, Part A: Applications*, 1–23, (2024). [CrossRef]

[20] Patil, P.M. and Benawadi, S. Bioconvective Casson–Williamson nanoliquid flow past a rough, slender cylinder: inclined magnetic field effect. *Multiscale and Multidisciplinary Modeling, Experiments and Design*, 8, 285, (2025). [CrossRef]

[21] Sagadevan, P., Raju, U., Murugesan, M., Fernandez-Gamiz, U. and Noeiaghdam, S. Chemical reactions with the Casson nanofluid flow by the bioconvective behavior of microorganisms

over a spinning disc. *Heliyon,* 11(1), e41238, (2025). [CrossRef]

[22] Dharmaiah, G., Balamurugan, K.S., Saxena, H., Fernandez-Gamiz, U., Noeiaghdam, S., Kumar, M.D. and Raju, C.S.K. Exploration of physical characteristics of gyrotactic microorganisms and Cattaneo-Christov heat flux past a cone and a wedge with thermal radiation. *Case Studies in Thermal Engineering*, 68, (2025). [CrossRef]

[23] Motsa, S.S. A new spectral local linearization method for nonlinear boundary layer flow problems. *Journal of Applied Mathematics,* 2013(1), 423628, (2013). [CrossRef]

[24] Otegbeye, O. and Motsa, S.S. A paired quasilinearization method for solving boundary layer flow problems. In Proceedings, *International Conference on Frontiers in Industrial and Applied Mathematics (FIAM),* 030020, Himachal Pradesh, India, (2018). [CrossRef]

[25] Meena, O.P. Mixed convection nanofluid flow over a vertical wedge saturated in porous media with the influence of thermal dispersion using Lie group scaling. *Computational Thermal Sciences: An International Journal,* 12(3), 191-205, (2020). [CrossRef]

[26] Meena, O.P. Mixed convection nanofluid flow over a vertical wedge saturated in a porous medium with influence of double dispersion using Lie group scaling. *Special Topics & Reviews in Porous Media: An International Journal,* 11(3), 297–311, (2020). [CrossRef]

[27] Meena, O.P. Mixed convection flow over a vertical cone with double dispersion and chemical reaction effects. *Heat Transfer,* 50(5), 4516-4534, (2021). [CrossRef]

[28] Meena, O.P., Janapatla, P. and Srinivasacharya, D. Influence of Soret and Dufour on mixed convection flow across a vertical cone. *Heat Transfer,* 50(8), 8280-8300, (2021). [CrossRef]

[29] Meena, O.P., Janapatla, P. and Meena, M.K. Influence of thermal dispersion and chemical reaction on mixed convection flow over a vertical cone saturated porous media with injection/suction. *Mathematical Models and Computer Simulations,* 14, 172–185, (2022). [CrossRef]

[30] Trivedi, M. and Ansari, M.S. Unsteady Casson fluid flow in a porous medium with inclined magnetic field in presence of nanoparticles. *The European Physical Journal Special Topics,* 228, 2553–2569, (2019). [CrossRef]

[31] Imtiaz, M., Hayat, T. and Alsaedi, A. Mixed convection flow of Casson nanofluid over a stretching cylinder with convective boundary conditions. *Advanced Powder Technology,* 27(5), 2245-2256, (2016). [CrossRef]

[32] Madhu, M. and Pasupula, M. Thermal radiation on three dimensonal Casson nanofluid flow with convective boundary layer via stretching sheet. *Tuijin Jishu/Journal of Propulsion Technology,* 44(6), 676-689, (2023).

[33] Saleem, M., Al-Zubaidi, A., Tufail, M.N., Fiaz, Z. and Saleem, S. Exploration of numerical simulation for unsteady Casson nanofluid thin film flow over stretching surface with mixed convection effects using Buongiorno's nanofluid model. *ZAMM-Journal of Applied Mathematics and Mechanics/Zeitschrift für Angewandte Mathematik und Mechanik,* 104(12), e202400165, (2024). [CrossRef]

[34] Kumar, V., Ram, P. and Sharma, K. Inclined magnetised convective dissipation of radiative Casson nanofluid in porous medium with Soret effect. *The European Physical Journal Special Topics,* (2025). [CrossRef]

[35] Aboel-Magd, Y., Basem, A., Farooq, U., Fatima, N., Noreen, S., Waqas, H. et al. Computational modeling of thermal radiation and activation energy effects in Casson nanofluid flow with bioconvection and microorganisms over a disk. *International Journal of Thermofluids,* 23, 100735, (2024). [CrossRef]

[36] Gubena, T. and Ibrahim, W. Mixed convection flow of Casson nanofluid over a nonlinearly stretching sheet with entropy generation, non-Fourier heat flux, and non-Fickian mass diffusion. *AIP Advances*, 15(3), 035329, (2025). [CrossRef]

[37] Joshi, A. The combined effect of magnetic field and viscous dissipation on the boundary layer flow over a permeable stretching sheet in a casson nanofluid with convective boundary condition. *International Journal of Statistics and Applied Mathematics*, 5(2), 117-130, (2020).

[38] Farooq, U., Waqas, H., Alhazmi, S.E., Alhushaybari, A., Imran, M., Sadat, R. et al. Numerical treatment of Casson nanofluid Bioconvectional flow with heat transfer due to stretching cylinder/plate: Variable physical properties. *Arabian Journal of Chemistry*, 16(4), 104589, (2023). [CrossRef]

[39] Hussain, Z., Khan, W.A., Irfan, M., Muhammad, T., Eldin, S.M., Waqas, M. and Narayana, P.V.S. Interaction of gyrotactic moment of microorganisms and nanoparticles for magnetized and chemically reactive shear-thinning fluid with stratification phenomenon. *Nanoscale Advances*, 5, 6560-6571, (2023). [CrossRef]

[40] Gupta, S. and Sharma, K. Numerical simulation for magnetohydrodynamic three dimensional flow of Casson nanofluid with convective boundary conditions and thermal radiation. *Engineering Computations*, 34(8), 2698-2722, (2017). [CrossRef]

[41] Mahmood, A., Jamshed, W. and Aziz, A. Entropy and heat transfer analysis using Cattaneo-Christov heat flux model for a boundary layer flow of Casson nanofluid. *Results in Physics*, 10, 640-649, (2018). [CrossRef]

[42] Rao, M.E., Sankari, M.S, Nagalakshmi, Ch. and Rajkumar, S. On the role of Bioconvection and activation energy for MHD-Stretched flow of Williamson and Casson nanofluid transportation across a porous medium past a permeable sheet. *Journal of Nanomaterials*, 2023(1), 995808, (2023). [CrossRef]

[43] Sangeetha, E. and De, P. Bioconvective Casson nanofluid flow toward stagnation point in non-Darcy porous medium with buoyancy effects, chemical reaction, and thermal radiation. *Heat Transfer*, 52(2), 1529-1551, (2023). [CrossRef]

Mathematical Modelling and Numerical Simulation with Applications (MMNSA)
(https://dergipark.org.tr/en/pub/mmnsa)

How to cite this article: Fayaz, T., Ansari, M.S., Otegbeye, O. & Trivedi, M. (2025). Flow of non-Newtonian fluid with convective conditions in Darcy-Forchheimer media: an unsteady case. *Mathematical Modelling and Numerical Simulation with Applications*, 5(2), 451-471. https://doi.org/10.53391/mmnsa.1548410